ChemComm

COMMUNICATION

View Article Online
View Journal | View Issue

Cite this: *Chem. Commun.*, 2025, **61**, 16226

Received 27th May 2025,
Accepted 11th September 2025

DOI: 10.1039/d5cc02935j

rsc.li/chemcomm

Spatially resolved *operando* X-ray diffraction for mapping heterogeneities in Li-ion single-layer pouch cells

Ashok S. Menon, [ae] Stephen W. T. Price, [*be] Muhammad Ans, [ae] Nickil Shah, [ae] Narayan Simrit Kaur, [ae] Pol Salles, [c] Innes McClelland, [de] Andrew M. Beale, [bfg] Simon D. M. Jacques, [b] Serena A. Cussen [de] and Louis F. J. Piper [*ae]

The electrochemical degradation of Li-ion batteries occurs over different spatial and temporal scales. This work demonstrates how *operando* synchrotron X-ray diffraction can be used to study degradation in Li-ion battery materials by mapping component-specific crystallographic structure evolution across a single-layer pouch full cell in real-time, enabling quantification of structural degradation processes in Li-ion battery cells from the atomic to macroscopic scale.

Degradation processes in Li-ion batteries can be broadly classified into those happening at the atomic, microscopic and macroscopic scale.[1] *Operando* X-ray diffraction (XRD) is the method of choice to study cycling-induced structure changes in Li-ion battery cells, as it provides direct real-time crystallographic information of the cell components in a non-destructive manner.[2] However, these studies are often localised investigations, where the X-ray beam is focused on a region (determined by X-ray beam size) close to the cell centre, whose electrochemical behaviour may or may not represent the overall cell behaviour. Li-ion cells/batteries have been reported to behave heterogeneously, with different regions of the cell showing varying degrees of electrochemical activity. This can originate from multiple factors including particle cracking, electrolyte depletion, electrode misalignment, improper cell sealing *etc.*, all of which can also exacerbate electrochemical performance degradation. Therefore, there is a need to identify and quantify the crystallographic evolution of different cell components over the entire cell, for example by *operando* XRD mapping.[3] This is crucial to develop an accurate picture of the overall cell degradation and becomes increasingly relevant when studying larger prismatic and cylindrical cells, where the propensity for heterogeneous behaviour is higher.[4–10]

Academic investigations of electrochemical performance degradation often use coin and/or single-layer pouch (SLP) cells. The latter enables reproducible practically relevant investigations of electrochemical performance and degradation mechanisms.[11] SLP cells are also ideal for *operando* X-ray measurements as they can be directly studied without any modifications that aid X-ray transmission, even using laboratory instruments,[12,13] provided the electrode active material loadings are sufficiently high. With the development of fourth-generation synchrotron sources and advanced data analytics tools, *operando* XRD mapping is gradually being adopted by the battery research community. However, complexity in terms of principle, instrumentation, and data analysis presents a high barrier of entry for new researchers. Therefore, this work demonstrates how *operando* synchrotron XRD mapping can quantifiably track spatial crystallographic changes in the electrode bulk and identify electrode-/cell-level heterogeneities arising from factors such as improper electrolyte wetting and electrode stacking. To amplify such heterogeneities for demonstrative purposes, a model $LiNiO_2$–graphite SLP cell (Fig. S1a) was assembled with a slightly misaligned electrode stack and sealed without vacuum (full details in SI). *Operando* XRD mapping was performed on the ID31 beamline at the European Synchrotron Radiation Facility (ESRF, Grenoble, France) using a 95 keV X-ray beam as the cell was charged to 4.5 V. *Operando* maps were measured with a pixel size of 100 μm × 600 μm with a XRD data collection time of 0.01 s per pixel, resulting in approx. 15 min per map of the SLP cell. High-resolution maps, with a pixel size of 100 μm × 100 μm, were collected at the open-circuit-voltage (OCV) and fully charged (4.5 V) states.

[a] *WMG, University of Warwick, Coventry, CV4 7AL, UK. E-mail: louis.piper@warwick.ac.uk*
[b] *Finden Ltd., Building R71, Rutherford Appleton Laboratory, Harwell, Oxford, OX11 0QX, UK. E-mail: stephen@finden.co.uk*
[c] *ESRF, 71 Avenue des Martyrs, 38043 Grenoble Cedex 9, France*
[d] *School of Chemistry, University College Dublin, Belfield, Dublin 4, Ireland*
[e] *The Faraday Institution, Harwell Science and Innovation Campus, Didcot, OX11 0RA, UK*
[f] *Department of Chemistry, 20 Gordon Street, University College London, London, WC1H 0AJ, UK*
[g] *Research Complex at Harwell, Rutherford Appleton Laboratory, Harwell Science and Innovation Campus, Harwell, Didcot, OX11 0FA, UK*

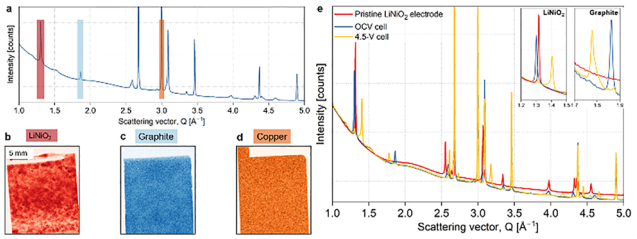

Fig. 1 (a) Averaged XRD pattern obtained from the mapped pixels across the SLP cell at the OCV state. XRD intensity maps from selected ROIs that have contributions from (b) $LiNiO_2$, (b) graphite and (c) copper. The ROIs in plot (a) are colour-coded to the maps below – red: $LiNiO_2$, blue: graphite, and brown: copper. The scale bar in (b) is also common to (c) and (d). (e) Averaged XRD data from a pristine $LiNiO_2$ cathode (red), and the SLP cell at OCV (blue) and charged states (yellow). ROIs corresponding to LNO and graphite are shown in the insets.

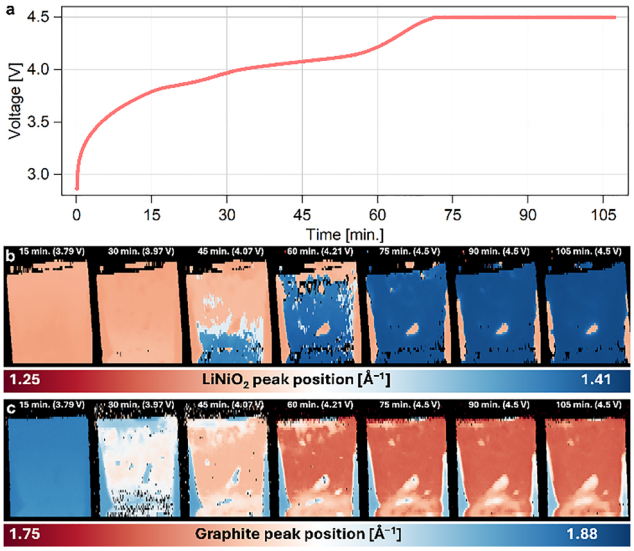

Fig. 2 (a) The electrochemical voltage *vs.* time profile from the *operando* experiment. Maps of the distribution of the (b) $LiNiO_2$ and (c) graphite peak positions representing the state of lithiation (where red and blue corresponds to higher and lower Li content, respectively) at selected charging stages.

Relevant experimental details about the cell and *operando* setup (Fig. S1b), including the data processing and analysis, are included in the SI.

Fig. 1a shows the XRD data averaged across the entire SLP cell in the OCV state. $LiNiO_2$ (LNO) cathode, graphite anode and the (Al and Cu) current collectors dominate, with non-crystalline cell components such as the pouch and separator having diffuse contributions to the overall intensity (Fig. S2a). The electrolyte may also lead to X-ray scattering intensities, predominantly in the low Q (scattering vector) region.[14] Fig. 1b–d are the XRD intensity maps from selected Q regions of interest (ROIs) focused on the LNO (003), graphite (002), and Cu (111) reflections, respectively, in Fig. 1a, and represent the spatial distribution of each phase, thereby (non-destructively) imaging the associated component within the cell. It is not possible to obtain a clear map of the Al current collector as the pouch cell material also contains Al (Fig. S2a). The intensity variations within the LNO map indicate the distribution of active material is not uniform across the electrode. This is rational considering that the cathode was manually prepared using the draw-down method, as opposed to the anode, which was fabricated using a roll-to-roll pilot-line coater. Fig. 1e shows the averaged XRD diffraction data from the cell at the OCV and charged (4.5 V) states, compared to a pristine LNO cathode. The LNO 003 reflection (left inset) in the OCV-cell data is at a lower Q value compared to the pristine cathode due to the incomplete re-lithiation during the previous cycle carried out to check the cell. Upon charging to 4.5 V, LNO shows the expected transformation from the parent hexagonal (H1) phase to the H3 phase (at 1.405 $Å^{-1}$).[15,16] A small amount of the preceding intermediate hexagonal (H2) phase is also observed, suggesting that delithiation has not occurred uniformly across the cathode. Concurrent changes are also observed in graphite, which predominantly exist in the LiC_{12} phase at the end of charge, with a small shoulder towards higher Q values signifying the presence of other graphite phases of lower lithiation.[17,18] This is expected as the heterogeneity in the cathode delithiation will undoubtedly affect the spatial anode lithiation.

Fig. 2a shows the voltage vs time profile during the *operando* experiment. Due to the deliberately non-optimal manufacture of the SLP to amplify heterogeneous behaviour, its electrochemical performance during the first charge is poorer compared to a properly built SLP of similar electrode chemistry, as reported in our previous work.[19] Fig. 2b shows the position of the LNO 003 reflection(s) at different stages of charging, determined by pseudo-Voigt peak fitting (see SI). The position of the LNO 003 reflection is dependent on the degree of delithiation, and therefore, directly probes the electrochemical activity of the cathode. Whilst initially fairly uniform, the peak position varies across the cathode as charging progresses – attributed to the combination of the inhomogeneous material loading, improper electrode stacking, and irregular contact between the electrolyte and electrode due to the absence of a vacuum seal. The right and left edges of the electrodes are completely inactive throughout charging, whilst an 'island' of reduced electrochemical activity appears towards the centre of the cell, where delithiation is slower, and is ascribed to weak electrolyte–electrode contact, whereas the edges are regions with electrode misalignment. Exemplar local XRD patterns from a line scan down the centre of the cell after charging for 45 mins are shown in Fig. S3 to illustrate the local variations in lithiation. Fig. 2c tracks the evolution of the graphite peak during charging, showing continuous progression towards lower Q values, and ending with the peak position corresponding to the LiC_{12} phase (red regions), with traces of intermediate phases such as LiC_{30} and LiC_{18} (marked by white regions in Fig. 2c). The LiC_6 phase is not reached as the lithiation does not progress to that extent. Thus, *operando* XRD mapping, even *via* simple peak fitting, can track heterogeneous electrochemical behaviour in the cell, and correlate it with macroscopic defects.

Fig. 3 contains four sets of maps, which shows the evolution of the refined scale factors of the LNO H2 and H3 phases, and the corresponding unit cell parameters. These data were obtained by Rietveld analysis of the XRD data collected at each pixel. The structural transition from the H2 to the H3 phase, expectedly, directly correlates with the peak position data in Fig. 2b. The inactivity of the edge regions and the retarded behaviour of the central region is observed *via* differences in the H2 to H3 transformation. At the edges, no H3 phase is formed, whereas in the central region, the formation of the H3 phase lags behind the rest of the cell (hence the observation of the small amounts of the H2 phase in charged-cell data in Fig. 1e). The evolution of the LNO unit cell parameters, obtained by fitting a $R\bar{3}m$ unit cell to each XRD data, conform to expected behaviour; the *a* parameter shows a gradual decrease before plateauing, whereas the *c* parameter initially increases before collapsing to lower values simultaneously with the formation of the H3 phase. Once again, the heterogeneity in delithiation is directly reflected in the lattice parameter evolution.

Fig. S4 shows the analogous anode maps with the scale factors of the different (lithiated) graphite phases, modelled using the graphite, LiC_{30}, LiC_{18} and LiC_{12} phases. The inactivity of the misaligned edge regions of the anode is evident from it remaining in the graphite phase (Fig. S4a). Interestingly, the central 'island' of inactivity is not visible, and implies that there is some (electrochemical) contact between the electrodes here, albeit weak. Since the lithiation of graphite results in a faster, more noticeable change in its XRD peak positions than the delithiation of LNO, the effects of charging are visible earlier than in the LNO data.

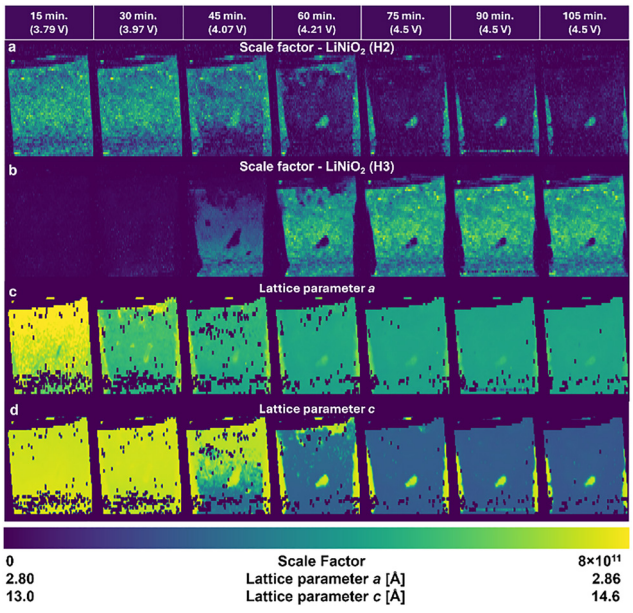

Fig. 3 Maps of different cathode parameters obtained from XRD data fitting: $LiNiO_2$ (a) H2 and (b) H3 phase scale factors, and (c) and (d) average unit cell parameters. The time and approx. voltage corresponding to each map is also mentioned at the top.

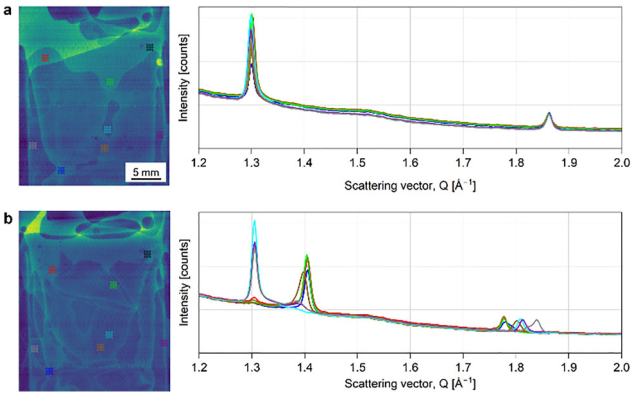

Fig. 4 XRD intensity map of the (a) OCV and (b) 4.5-V charged cell, corresponding to the *Q* range, 1.42–1.6 $Å^{-1}$. (b) Averaged XRD data from the 8 ROIs highlighted in the maps.

With the recent developments in synchrotron XRD instrumentation, it is also possible to track variations in the background and diffuse scattering features in the XRD data during cycling. Although this is particularly complex for dynamic, multi-component electrochemical systems, requiring foundational systematic studies to isolate contributions from individual components, it has the potential to provide further insights into the underlying processes. A preliminary example of how tracking variations in the diffuse scattering and background may provide insights about variations in the electrochemical behaviour is presented in Fig. 4. It shows the high-resolution XRD intensity maps of the OCV and charged cells corresponding to the 1.42–1.60 $Å^{-1}$ range; sufficiently away from the direct beam while not having any contributions from the electrodes. Contributions from the pouch material and separator (Fig. S2a), are present but expected to be invariant during cycling. Intriguingly, there are strong spatial intensity variations across the cell at OCV, which also notably change after charging. This is reflected in the averaged XRD data from the 8 ROIs, as shown in the panels to the right of their corresponding maps. The ROIs (1 mm^2, 100 pixels) correspond to regions with visible intensity variations. These patterns show the expected intensity variations in the LNO reflections (due to inhomogeneous active material loading), while the graphite data are highly comparable. In the charged cell, the ROI patterns show significant variations. Three ROIs (cyan, violet and grey) specifically show reduced delithiation (based on the LNO (003) position) while occupying regions with lower diffuse scattering intensities on the map. Based on these observations, it may be cautiously hypothesised that the scattered intensity in the 1.42–1.60 $Å^{-1}$ range is influenced by electrolyte–electrode interactions. For example, as the electrolyte directly participates in the electrochemical reactions, it is rational that its scattering intensity contributions are altered during charging. Additionally, the LNO cathode when charged to 4.5 V, will evolve oxygen, which can interact with the electrolyte to form gaseous CO_2 and CO, the build up of which can also alter the distribution of electrolyte within the SLP cell, explaining the changes in the

spatial intensity distribution after charging. The absence of a vacuum seal may also lead to inhomogeneous distribution of the electrolyte within the SLP cell. Whilst further systematic investigations are required to conclusively deconvolute the contribution of electrolyte to the overall XRD data, this is an encouraging example as to how electrolyte dynamics may also be characterised using *operando* XRD mapping, offering new research avenues to take advantage of the advanced synchrotron X-ray facilities worldwide.

Operando XRD mapping is presented as a technique to obtain spatially resolved component-specific structural information during electrochemical cycling of lab-standard SLP full cells. The cell was deliberately fabricated without proper electrode stacking and vacuum sealing to amplify spatial heterogeneities. This served as an ideal example to illustrate how single-point/region investigations may not provide an accurate description of the overall cell behaviour. These fast *operando* studies are feasible due to recent developments in synchrotron X-ray brightness and detector sensitivity, and along with the direct interface of the electrochemical control with the beamline, render this type of measurement accessible to all users. Preliminary work on how analysing the changes in the background and diffuse scattering features in the *operando* XRD data may provide additional insights into the behaviour of the cells is also demonstrated, and offers exciting directions for future work.

ASM and SWTP were responsible for data collection, processing, analysis and manuscript writing. MA, NS and PS prepared the cells and data collection. NSK and IM synthesized the cathode material. AMB, SDMJ, SWTP, SAC and LFJP were responsible for funding acquisition and conceptualization. All authors contributed to the discussion of the results.

This work was supported by the Faraday Institution FutureCat project (FIRG017 and FIRG065). SWTP acknowledges the Faraday Institution for funding (FIIF-020). The Research Pouch Cell Manufacture (FIRG062) and Degradation (FIRG060) projects are also acknowledged. The ESRF is acknowledged for experimental time on beamline ID31 (CH-6918).

Conflicts of interest

There are no conflicts to declare.

Data availability

Raw X-ray data generated at the ESRF large-scale facility are available at **https://doi.org/10.15151/ESRF-ES-1596523572** from 2027. See DOI: **https://doi.org/10.1039/d5cc02935j**.

Notes and references

1 J. S. Edge, S. O'Kane, R. Prosser, N. D. Kirkaldy, A. N. Patel, A. Hales, A. Ghosh, W. Ai, J. Chen and J. Yang, *et al.*, *Phys. Chem. Chem. Phys.*, 2021, **23**(14), 8200–8221.
2 W. Li, D. M. Lutz, L. Wang, K. J. Takeuchi, A. C. Marschilok and E. S. Takeuchi, *Joule*, 2021, **5**(1), 77–88.
3 V. Gonzalez, M. Cotte, F. Vanmeert, W. de Nolf and K. Janssens, *Chem. – Eur. J.*, 2020, **26**(8), 1703–1719.
4 A. S. Leach, A. V. Llewellyn, C. Xu, C. Tan, T. M. M. Heenan, A. Dimitrijevic, K. Kleiner, C. P. Grey, D. J. L. Brett and C. C. Tang, *et al.*, *Front. Chem. Eng.*, 2022, **3**, 794194.
5 T. Bond, R. Gauthier, G. King, R. Dressler, J. J. Abraham and J. R. Dahn, *J. Electrochem. Soc.*, 2024, **171**(11), 110514.
6 H. Charalambous, D. P. Abraham, A. R. Dunlop, S. E. Trask, A. N. Jansen, T. R. Tanim, P. R. Chinnam, A. M. Colclasure, W. Xu and A. A. Yakovenko, *et al.*, *J. Power Sources*, 2021, **507**, 230253.
7 M. J. Mühlbauer, A. Schökel, M. Etter, V. Baran and A. Senyshyn, *J. Power Sources*, 2018, **403**, 49–55.
8 D. R. Sørensen, R. Gordon, A. Smith, I. Kantor and M. R. V. Jørgensen, *Chem. Mater.*, 2024, **36**(21), 10871–10885.
9 H. Liu, S. Kazemiabnavi, A. Grenier, G. Vaughan, M. Di Michiel, B. J. Polzin, K. Thornton, K. W. Chapman and P. J. Chupas, *ACS Appl. Mater. Interfaces*, 2019, **11**(20), 18386–18394.
10 A. Mikheenkova, A. Schökel, A. J. Smith, I. Ahmed, W. R. Brant, M. J. Lacey and M. Hahlin, *J. Power Sources*, 2024, **599**, 234190.
11 M. D. L. Garayt, M. B. Johnson, L. Laidlaw, M. A. McArthur, S. Trussler, J. E. Harlow, J. R. Dahn and C. Yang, *J. Electrochem. Soc.*, 2023, **170**(8), 080516.
12 A. S. Menon, N. Shah, J. A. Gott, E. Fiamegkou, M. J. W. Ogley, G. J. Páez Fajardo, N. Vaenas, I. Ellis, N. Ravichandran and P. Cloetens, *et al.*, *PRX Energy*, 2024, **3**(1), 013004.
13 M. J. W. Ogley, A. S. Menon, G. C. Pandey, G. J. Páez Fajardo, B. J. Johnston, I. McClelland, V. Majherova, S. Huband, D. Tripathy and I. Temprano, *et al.*, *Joule*, 2025, **9**(1), 101775.
14 L. Vitoux, M. Reichardt, S. Sallard, P. Novák, D. Sheptyakov and C. Villevieille, *Front. Energy Res.*, 2018, **6**, 76.
15 W. Li, J. N. Reimers and J. R. Dahn, *Solid State Ionics*, 1993, **67**(1), 123–130.
16 H. Li, N. Zhang, J. Li and J. R. Dahn, *J. Electrochem. Soc.*, 2018, **165**(13), A2985–A2993.
17 T. Ohzuku, Y. Iwakoshi and K. Sawai, *J. Electrochem. Soc.*, 1993, **140**(9), 2490.
18 S. Schweidler, L. de Biasi, A. Schiele, P. Hartmann, T. Brezesinski and J. Janek, *J. Phys. Chem. C*, 2018, **122**(16), 8829–8835.
19 M. Ans, G. C. Pandey, I. McClelland, N. Gollapally, H. Gillions, B. I. Johnston, M. J. Ogley, J. A. Gott, E. Fiamegkou, V. Celorrio, P. K. Thakur, T.-L. Lee, S. A. Cussen, A. S. Menon and L. F. J. Piper, *Adv. Energy Mater.*, 2025, 2500597.